

Effect of electron–phonon interaction on the formation of one-dimensional electronic states in coupled Cl vacancies

Bruno Schuler,^{1,*} Mats Persson,^{2,3} Sami Paavilainen,⁴ Niko Pavliček,¹ Leo Gross,¹ Gerhard Meyer,¹ and Jascha Repp⁵

¹*IBM Research – Zurich, Säumerstrasse 4, 8803 Rüschlikon, Switzerland*

²*Surface Science Research Centre, Department of Chemistry, University of Liverpool, Liverpool, L69 3BX, United Kingdom*

³*Department of Applied Physics, Chalmers University of Technology, SE 41296, Göteborg, Sweden*

⁴*Department of Physics, Tampere University of Technology, 33720 Tampere, Finland*

⁵*Institute of Experimental and Applied Physics, University of Regensburg, 93053 Regensburg, Germany*

(Dated: March 6, 2022)

The formation of extended electron states in one-dimensional nanostructures is of key importance for the function of molecular electronics devices. Here we study the effects of strong electron–phonon interaction on the formation of extended electronic states in intentionally created Cl vacancy pairs and chains in a NaCl bilayer on Cu(111). The interaction between the vacancies was tailored by fabricating vacancy pairs and chains of different orientation and separation with atomic precision using vertical manipulation. Small separation of divacancies led to the formation of symmetric and antisymmetric vacancy states and localized interface-states. By scanning tunneling spectroscopy (STS) we measured their energy splitting and broadening as a function of the inter-vacancy separation. Unexpectedly, the energy splitting between the vacancy states is enlarged by level repulsion resulting from phonon dressing of the electronic states, as evidenced by theory. Already for a few coupled vacancies we observe an emerging band structure of the defect band.

One-dimensional nanostructures assembled from single metal atoms and molecules on surfaces are of great fundamental and technological interest as their electronic states exhibit a wealth of new quantum phenomena that might be exploited in future molecular electronics devices¹. Some examples of such phenomena identified by scanning tunneling microscopy (STM) and spectroscopy (STS) include metal-atom chains exhibiting ‘particle-in-box’ states², bistable antiferromagnetism³, Tomonaga–Luttinger liquid behaviour⁴, and signs of Majorana spinors⁵. The formation of extended or band-like electronic states in metal-atom and molecular chains on surfaces has been widely studied experimentally^{6–10}, but potentially interesting effects of strong electron–phonon coupling on these states, such as, for instance, polaronic effects, have attracted much less attention. A notable exception is the observation of coherent electron–phonon states and the breakdown of the Born–Oppenheimer approximation in oligothiophene molecular chains¹¹. In the electronically adiabatic regime, where the Franck–Condon principle is applicable, the electron–phonon coupling results in vibronic satellite structures. How these vibronic effects influence the delocalization of an injected electron in a one-dimensional nanostructure is an open question, in particular when the electron–phonon coupling is so strong that these effects dominate.

Here we address this question in a combined experimental and theoretical study of coupled electronic states localized at intentionally created Cl divacancies

and vacancy chains in a NaCl bilayer on Cu(111). The Cl vacancies provide a quantum-well structure that could be created with atomic precision using the STM tip^{12,13}. The energies of the electronic states formed in these structures by injection of an electron from the tip of an STM and their spatial behaviour on the atomic scale were resolved by STS and analyzed using simple models. Our findings have ramifications for the formation of extended states from coupled adsorbate or confined defect states (such as in dopants¹⁴ or dangling bonds¹⁵) in semiconductors and ionic crystals. Hence, it could improve the understanding of polaronic effects in coupled quantum systems, such as quantum dots^{16–21}, charge-based qubits^{22,23} and quantum cellular automata²⁴.

Coupled, individual Cl vacancies in a NaCl bilayer on a Cu(111) surface are ideal model systems to study the effect of strong electron–phonon coupling on the delocalization of electronic states. First, Cl monovacancies are atomically well-defined and highly symmetric defects. They feature two distinct electronic states: an unoccupied vacancy state (VS) that is strongly coupled to optical phonons in the film and a localized interface-state (LIS) with a negligible electron–phonon coupling^{25,26}. The electronic coupling between VSs or LISs of different vacancies can be tuned in a controlled way by the lateral spacing between vacancies with atomic precision²⁷. Finally, Cl vacancies feature a much higher stability against inelastic excitations than adsorbates²⁸. Cl vacancies could even be filled with

other atoms²⁹. Hence, they allow us to explore artificial coupled quantum systems with great control.

In a previous study³⁰, single Cl vacancies in a NaCl bilayer on copper surfaces were characterized in detail. A Cl vacancy in the outermost layer of this supported NaCl bilayer is analogous to the widely studied and well-known colour centers in bulk NaCl³¹ with one key difference: the localized VS is unoccupied because the electron can tunnel into unoccupied metal states. The unoccupied VS then gives rise to a positively charged vacancy and an attractive potential that is able to split off a LIS from the free-electron-like interface-state band of the NaCl/Cu(111)³². This LIS was observed as a narrow resonance just below the bottom of the interface-state band in the differential conductance (dI/dV) spectra, whereas the VS showed up as a broad negative ion resonance at a sample voltage of about 2.8 V in dI/dV spectra. The negative ion resonance was found to have a large Gaussian broadening (full-width half maximum (FWHM) of $\sigma = 0.27$ V) because of the strong electron-phonon coupling of the electron in the VS to optical phonons in the NaCl bilayer. Despite this strong coupling corresponding to an estimated Huang-Rhys parameter of about $S = 30$, the associated relaxation energy of the electron in the VS is not large enough to prohibit tunneling into unoccupied metal states and to allow the formation of a stable occupied VS state corresponding to a localized polaron. In contrast to the VS, the LIS was found to be dominated by lifetime broadening with a negligible phonon broadening in the dI/dV spectra, owing to the efficient screening of the electron-phonon interaction by the metal electrons.

The atomically precise locations of intentionally created Cl divacancies in a NaCl bilayer on Cu(111) were resolved unambiguously using noncontact atomic force microscopy (AFM) with CO-terminated tips (CO tips)^{33,34}. Divacancies in the ninth-nearest-neighbour (9NN), 6NN, 5NN, 4NN, 3NN and 2NN configurations (see schematic in Fig. 1a) were created from two Cl vacancies close to each other but not in the vicinity of any other vacancies or defects. Constant-height AFM images of the 5NN to 3NN divacancies and of a single vacancy are shown in Fig. 1b-e. The electronic structure of the VSs and the LISs of the divacancies were characterized by constant-height $dI/dV(x, V)$ maps along the line connecting the two vacancies in Fig. 1g-j and Fig. 1l-o, respectively. All dI/dV data shown are recorded using Cu-terminated tips. For the 4NN, 3NN and 2NN³⁵ divacancy configurations, two peaks with Gaussian line shapes were observed around 2.8 V. The $dI/dV(x, V)$ maps show that the state at lower energy is localized between the vacancies (symmetric), whereas the state at higher energy has a nodal plane between them (antisymmetric), in analogy with the bonding

and antibonding orbitals of the hydrogen molecule. Similarly, the divacancy LISs were also observed to split into a symmetric and an antisymmetric state. However, for small vacancy separations, the latter state lies above the NaCl/Cu(111) interface band onset at $\varepsilon_B = -230$ mV and overlaps with the band continuum. Hence, only the symmetric state is observed as a well-defined peak in dI/dV . The splitting of both the VSs and LISs was found to increase with decreasing inter-vacancy distance. Tab. S1 summarizes the observed peak positions and energy splittings of the VSs and LISs.

To study the delocalization of VSs and LISs further, short one-dimensional arrays of N vacancies, referred to in the following as vacancy chains, were created in the 5NN (apolar NaCl direction) and the 3NN (polar NaCl direction) configuration. They were also characterized by constant-height CO tip AFM images (Fig. 2a,c). For the 5NN chains, the LISs form one-dimensional quantum-well states, observed as distinct resonances in dI/dV , with an increasing integer number of nodal planes with voltage (see Fig. 2b and Fig. S2). Surprisingly, also broad resonances are observed up to 200 – 300 mV above the interface-state band onset. These quasi-bound LISs have a lower height in dI/dV , owing to the increased lifetime broadening compared to the bound LISs. This originates from the additional decay channel into the interface-state band. Furthermore, the energy position of the ground-state LIS does not change significantly from the $N = 4$ to the $N = 6$ chain and seems to converge to about -0.33 V. The VSs in the 5NN chains only show a single resonance peak at about 2.7 V because of the weak electronic interaction between the VSs at these large intervacancy distances (cf. Fig. 1h). In contrast, the 3NN chains displayed in Fig. 2c have a significant interaction between the VSs and exhibit several resonances, as shown in Fig. 2d. The increasing number of nodal planes with voltage shows that the VSs are delocalized over these chains despite the strong electron-phonon coupling. In addition, the band width of VSs increases with chain length N , and is more or less saturated at 0.54 V for the $N = 5$ chain. Interestingly, the level broadening decreases for longer chains as displayed in Fig. 3a. This finding can be rationalized by the larger spatial extent of the eigenstates, which decreases their relaxation energy and accordingly the effective electron-phonon coupling.

In the following, the VS energies of the 3NN chains are compared with the results from a simple tight-binding (TB) model. First, we assume that each vacancy in the chain has an on-site energy ε_0 and is coupled to its next neighbour(s) with a hopping term $-t$, as sketched in Fig. 3b. By adjusting the free fitting parameters ε_0 and t to the experimental mono- and divacancy VS energies, one can calculate the energy

levels for different chain lengths as shown in Fig. 3e. In comparison with the experimental energy spectrum, depicted in Fig. 3d, the level spacings for each chain could be roughly reproduced, but the TB model does not capture the shift of the band center towards lower energies with increasing chain length. This shift can be explained by the electrostatic interaction between adjacent vacancies that deepens the potential at each vacancy and therefore lowers the on-site energy. To account for the energy shift we introduce the parameter δ , which is the on-site energy shift due to a neighbouring vacancy (see Fig. 3c). The resulting energy levels of this extended TB model are shown in Fig. 3f. The calculated energy spectrum now agrees very well with the experimentally observed VS levels of the chains.

So far, the strong electron–phonon coupling, as shown by the large broadening of the VSs, was neglected in our tight-binding models. The role of this coupling in the formation of delocalized states by a tunneling electron in vacancy pairs (and chains) needs to be investigated. Here, we use a simple generalization of the electron–phonon interaction model of the single vacancy³⁰ to vacancy pairs and chains. As detailed in the SI, the direct electronic interactions between the VSs are described by a simple tight-binding model, and each VS is coupled linearly to the phonon modes of the NaCl film. As we will show next, in this model, the strong electron–phonon coupling has a profound effect on the energy splitting and broadening of the vacancy states. This effect is illustrated here for a divacancy using appropriate parameters, where each single vacancy state is coupled to a single Einstein phonon mode. Here, the electronic interaction between the vacancies is large compared to the phonon energy, corresponding to an electronically adiabatic regime.

In Fig. 4a, the adiabatic potential energy surfaces (PES) of the singly occupied, divacancy states for symmetric displacements q_s (where $q_1 = q_2$) of the two Einstein phonon modes are shown. They are split by $2t$, where $-t$ is the direct electronic interaction between the VSs, and both have the same shape as for the adiabatic PES of a monovacancy. In contrast, along antisymmetric displacements q_{as} (where $q_1 = -q_2$) (Fig. 4b), the corresponding PESs exhibit an avoided crossing with a minimum energy gap of $2t$. This level repulsion will be shown to have a profound influence on the phonon broadening and the formation of delocalized states.

As for the single vacancy, the result for the phonon broadening of the tunneling through the divacancy states turns out to have a simple physical form in the prevailing strong electron–phonon coupling limit, as detailed in the SI. The phonon broadening is determined

by probabilities for vertical Franck–Condon transitions from the vibrational ground-state of the PES of the electronic ground-state to vibrational states on the two PESs for the divacancy states (gray arrows in Fig. 4c and d). In the strong electron–phonon coupling limit, the transition probabilities are dominated by the contribution from the linear electron–phonon coupling terms. The corresponding phonon broadenings are then simply obtained from the change in the divacancy energy levels $\tilde{\varepsilon}_b$ (bonding state) and $\tilde{\varepsilon}_a$ (antibonding state) with the Gaussian fluctuations of the energies $\delta\varepsilon_1$ and $\delta\varepsilon_2$ of the vacancy 1 and 2 from their mean value ε_0 due to the zero-point motions of the phonons. As shown in the SI, this result is also valid for more general phonon baths and electron–phonon couplings.

The strong coupling result for the phonon broadening of the divacancy states is illustrated in Fig. 4c and d. A symmetric fluctuation $\delta\varepsilon_s$ (where $\delta\varepsilon_1 = \delta\varepsilon_2$) results, as shown in Fig. 4c, in a linear dependence of $\tilde{\varepsilon}_b$ and $\tilde{\varepsilon}_a$ on $\delta\varepsilon_s$ with slope one, but they are split by $2t$. These Gaussian fluctuations then give rise to two overlapping Gaussian lineshapes centered at $\varepsilon_0 \pm t$ with a variance of $\langle \delta\varepsilon_s^2 \rangle$ for the local density of states (LDOS).

In contrast, the level repulsion results in a minimum energy separation $2t$ between $\tilde{\varepsilon}_b$ and $\tilde{\varepsilon}_a$ for an antisymmetric fluctuation $\delta\varepsilon_{as}$ (where $\delta\varepsilon_1 = -\delta\varepsilon_2$). Furthermore, $\delta\varepsilon_{as}$ breaks the symmetric and antisymmetric character of the two coupled VSs, and they tend to localize on each vacancy for $\delta\varepsilon_{as} \gg t$. The resulting LDOS from these Gaussian fluctuations, shown in Fig. 4d, consists of two relatively sharp, highly asymmetric lineshapes, with mean energies separated by more than the energy splitting $2t$. In general, the fluctuations $\delta\varepsilon_1$ and $\delta\varepsilon_2$ of the two vacancy energies will be a superposition of both $\delta\varepsilon_s$ and $\delta\varepsilon_{as}$. In the case of uncorrelated energy fluctuations $\langle \delta\varepsilon_1 \delta\varepsilon_2 \rangle = 0$, the LDOS is a convolution of the lineshape from $\delta\varepsilon_{as}$ with a Gaussian lineshape with a variance of $\langle \delta\varepsilon_{1,2}^2 \rangle / 2$ because $\delta\varepsilon_s$ and $\delta\varepsilon_{as}$ contribute equally to $\langle \delta\varepsilon_{1,2}^2 \rangle$, the variance of the single vacancy energy fluctuations. As the Gaussian shape dominates the broadening in such a convolution, the resulting LDOS as displayed in Fig. 4e has a similar shape as two Gaussians with a FWHM reduced by almost $1/\sqrt{2}$ as compared to an isolated vacancy. This decrease of the broadening in the uncorrelated case is the underlying reason why the observed broadenings of the levels of the chains decrease with chain size (see SI).

The two phonon modes considered here affect only one of the VSs each and result in uncorrelated vacancy site energy fluctuations. In reality, however, a given individual phonon mode may act on the energy of both vacancies in a symmetric or antisymmetric fashion

(consider e.g. the motion of an ion centered between two vacancies). Hence, partially correlated vacancy site energy fluctuations cannot be excluded. As shown in the SI, the two Einstein modes and their symmetric and antisymmetric fluctuations can serve as a basis for the description of any phonon bath and electron–phonon coupling. Our experimental results are consistent with the assumption of fully uncorrelated fluctuations of the two VSs. Interestingly, in the uncorrelated case, the LDOS, shown in Fig. 4e (red line), exhibits two peaks with an apparent separation that is substantially larger than the intrinsic splitting of $2t$. This result is a characteristic effect of the level repulsion between $\tilde{\varepsilon}_b$ and $\tilde{\varepsilon}_a$ and is in sharp contrast compared to a superposition of two monovacancy resonances separated by the intrinsic splitting (shown in Fig. 4e (blue line)). In the latter case, one would not be able to identify separate peaks due to the larger broadening and smaller splitting.

The enhancement of the apparent peak separation in the uncorrelated case over the intrinsic splitting is shown in Fig. 4f as a function of the scaled intrinsic energy splitting $2t/\sigma$, where σ is the broadening of a single VS. We define the apparent peak separation $\Delta\tilde{\varepsilon}$ as the separation between the centers of the two Gaussian lineshapes with broadening (FWHM) $\tilde{\sigma}$ fitted to the calculated LDOS. The relative enhancement $\Delta\tilde{\varepsilon}/2t$ of the apparent splitting is most important for small t . For large t , the splitting of divacancy energy levels approaches the intrinsic energy splitting of $2t$. As for the single vacancy level, the broadening of a divacancy level then scales with the square root of its relaxation energy (see SI).

The hopping terms t can be extracted from Fig. 4f by taking $\Delta\tilde{\varepsilon}$ equal to the observed splitting and using the single vacancy value 0.27 eV for σ . For example, $t = 0.11$ eV was obtained from $\Delta\tilde{\varepsilon} = 0.28$ eV for the 3NN divacancy. The values obtained for the hopping terms t are very reasonable as supported by density-functional theory (DFT) calculations of the unoccupied Kohn–Sham states of Cl divacancies in NaCl(2ML)/Cu(111). As shown in Fig. 4f, the calculated values for $2t$ of the various divacancy configurations are close to the values for the intrinsic splittings extracted from experimental data. However, the absolute divacancy energies are underestimated by the DFT calculations, as expected (see Fig. S3e).

The coupling between the LISs of Cl divacancies and chains were studied in a simple, multiple σ -wave scattering model of the interface-state scattering from the positively charged vacancies (see methods and SI). The results from this model, as indicated in Fig. 11-o, are able to fully capture the observed behavior of the coupled LISs. The absence of a LIS doublet below the

onset of the interface-state band is simply understood by the relatively strong interaction between the weakly bound LISs of the two vacancies at small intervacancy distances. With increasing distances between the vacancies, this interaction decreases, and a second LIS appears below the band onset. The observed symmetric character of the LIS below the band edge and antisymmetric character of the extended LIS above ε_B for the 3NN vacancy are also revealed in the calculated LDOS images (see Fig. S5). Furthermore, the obtained energies for the LISs of the vacancy chains are in excellent agreement with the experiments, as indicated in Fig. 2b.

In summary, from an AFM and STS study we find that the localized VSs and LISs at intentionally created Cl divacancies in a NaCl bilayer on Cu(111) form symmetric and antisymmetric states, in analogy to the bonding and antibonding orbitals of a hydrogen molecule. As expected, the energy splitting between these states increases with decreasing intervacancy distance. A comparison with theory shows that the energy splitting of the VSs is significantly enlarged by the strong coupling of the tunneling electrons with phonons in the NaCl film. Furthermore, VSs and LISs of vacancy chains form one-dimensional quantum-well states. The VS levels of the chains could be well described by a simple tight-binding model that takes the electrostatic interaction between neighbouring vacancies into account. The model provides also a microscopic understanding why the level broadening is reduced with increasing chain size. Already for about five coupled vacancies, a one-dimensional electronic band structure evolves.

METHODS

Sample preparation and Cl vacancy creation.

The experiments were carried out in a home-built low-temperature combined STM and AFM operated at 5 K. A Cu(111) single-crystal sample was cleaned by several sputtering and annealing cycles. NaCl was evaporated thermally, keeping the sample temperature at about 270 K, such that defect-free, (100)-terminated NaCl bilayer islands were formed^{36,37}. Bias voltages refer to the sample voltage with respect to the tip. In the spectroscopic measurements, the tunneling conductance dI/dV was recorded with conventional lock-in techniques with an ac bias amplitude of 25 mV at a frequency of 294 Hz. In the double-barrier tunneling junction geometry, the voltage drop across the insulating film will cause a voltage-dependent shift of the electronic levels. This tip-induced Stark shift is a few percent of the applied bias but depends only weakly on the tip distance. Therefore it is not considered here³⁰. The vacancies were created by bringing the Cu tip into controlled contact with the

NaCl surface. Thereby a Cl atom is transferred to the tip apex, as evidenced by a characteristic contrast change in STM images and a remaining depression at the predefined Cl site. Constant-height AFM images with a CO tip^{33,34} were recorded to identify the vacancy location and exclude the generation of other close-by defects. In addition, we measured the local contact potential difference on the polar film with Kelvin probe force microscopy to ensure that the defects are indeed Cl vacancies³⁸.

Theoretical calculations.

Density functional calculations. The electronic and geometric structure of the divacancies and vacancy chains in a NaCl bilayer on a Cu(111) surface were obtained using periodic density functional theory (DFT) calculations. We used the projector augmented wave (PAW) method^{39,40} as implemented in VASP⁴¹. The exchange-correlation energy was described by the optB86b+vdW approximation^{42,43}. The incommensurate growth of NaCl on Cu(111) was modeled by a super cell consisting of 90 Cu atoms and 32 Na and Cl atoms in each layer (4 layers of Cu and 2 layers of NaCl), which corresponds to about 2% mismatch of NaCl distances compared to those in bulk NaCl.

Phonon broadening model. This simple model detailed in the SI contains two key parameters: the phonon broadening σ (FWHM) of the single VS and the magnitude of the direct interaction energy $-t$ between the two VSs. The value for σ is determined from the observed broadening of 0.27 eV of the single vacancy VS. The values for t were adjusted to reproduce the observed energy splittings of the divacancy VSs and compared with results from the DFT calculations. For further information see the SI⁴⁴.

Interface-state band scattering model. The coupling between the LISs of Cl divacancies are modeled with a multiple σ -wave scattering model of the interface-state scattering from the vacancies. This model is detailed in the SI⁴⁴. The interface-state band is modeled by a 2D free-electron band with an effective mass m^* and a band onset ε_B . The values for $m^* = 0.46 m_e$ and $\varepsilon_B = -230$ meV of the interface-state band were taken from STM and STS measurements³⁷. The remaining parameter $\varepsilon_0 - \varepsilon_B$, determines the t -matrix element for σ -wave scattering and was fitted to the observed value of -19 meV for the LIS of the vacancy.

2. Niluis, N., Wallis, T. M. & Ho, W. Development of one-dimensional band structure in artificial gold chains. *Science* **297**, 1853–1856 (2002).
3. Loth, S., Baumann, S., Lutz, C. P., Eigler, D. M. & Heinrich, A. J. Bistability in atomic-scale antiferromagnets. *Science* **335**, 196–199 (2012).
4. Blumenstein, C. *et al.* Atomically controlled quantum chains hosting a Tomonaga-Luttinger liquid. *Nature Phys.* **7**, 776–780 (2011).
5. Nadj-Perge, S. *et al.* Observation of Majorana fermions in ferromagnetic atomic chains on a superconductor. *Science* **346**, 602–607 (2014).
6. Crain, J. N. & Pierce, D. T. End states in one-dimensional atom chains. *Science* **307**, 703–706 (2005).
7. Barke, I. *et al.* Low-dimensional electron gas at semiconductor surfaces. *Solid State Commun.* **142**, 617–626 (2007).
8. Fölsch, S., Yang, J., Nacci, C. & Kanisawa, K. Atom-by-atom quantum state control in adatom chains on a semiconductor. *Phys. Rev. Lett.* **103**, 096104 (2009).
9. Wang, S., Wang, W. & Lin, N. Resolving band-structure evolution and defect-induced states of single conjugated oligomers by scanning tunneling microscopy and tight-binding calculations. *Phys. Rev. Lett.* **106**, 206803 (2011).
10. Riss, A. *et al.* Local electronic and chemical structure of oligo-acetylene derivatives formed through radical cyclizations at a surface. *Nano Lett.* **14**, 2251–2255 (2014).
11. Repp, J., Liljeroth, P. & Meyer, G. Coherent electron-nuclear coupling in oligothiophene molecular wires. *Nature Phys.* **6**, 975–979 (2010).
12. Olsson, F. *et al.* Localization of the Cu(111) surface state by single Cu adatoms. *Phys. Rev. Lett.* **93**, 206803 (2004).
13. Fölsch, S., Martínez-Blanco, J., Yang, J., Kanisawa, K. & Erwin, S. C. Quantum dots with single-atom precision. *Nat. Nanotechnol.* **9**, 505–508 (2014).
14. Koenraad, P. M. & Flatté, M. E. Single dopants in semiconductors. *Nature Mat.* **10**, 91–100 (2011).
15. Schofield, S. *et al.* Quantum engineering at the silicon surface using dangling bonds. *Nature Commun.* **4**, 1649 (2013).
16. Lorke, A., Kotthaus, J. & Ploog, K. Coupling of quantum dots on GaAs. *Phys. Rev. Lett.* **64**, 2559–2562 (1990).
17. Hameau, S. *et al.* Strong electron-phonon coupling regime in quantum dots: Evidence for everlasting resonant polarons. *Phys. Rev. Lett.* **83**, 4152–4155 (1999).
18. Haider, M. B. *et al.* Controlled coupling and occupation of silicon atomic quantum dots at room temperature. *Phys. Rev. Lett.* **102**, 046805 (2009).
19. Sun, Z., Swart, I., Delerue, C., Vanmaekelbergh, D. & Liljeroth, P. Orbital and charge-resolved polaron states in CdSe dots and rods probed by scanning tunneling spectroscopy. *Phys. Rev. Lett.* **102**, 196401 (2009).
20. Leturcq, R. *et al.* Franck-Condon blockade in suspended carbon nanotube quantum dots. *Nature Phys.* **5**, 327–331 (2009).
21. Seufert, K. *et al.* Controlled interaction of surface quantum-well electronic states. *Nano Lett.* **13**, 6130–6135 (2013).
22. Andresen, S. E. *et al.* Charge state control and relaxation in an atomically doped silicon device. *Nano Lett.* **7**, 2000–2003 (2007).
23. Mujica-Martinez, C. A., Nalbach, P. & Thorwart, M. Organic π -conjugated copolymers as molecular charge qubits. *Phys. Rev. Lett.* **111**, 016802 (2013).

* bsc@zurich.ibm.com

1. Oncel, N. Atomic chains on surfaces. *J. Phys.: Condens. Matter* **20**, 393001 (2008).

24. Lent, C. S., Tougaw, P. D., Porod, W. & Bernstein, G. H. Quantum cellular automata. *Nanotechnology* **4**, 49 (1993).
25. Nilius, N., Wallis, T. & Ho, W. Influence of a heterogeneous Al₂O₃ surface on the electronic properties of single Pd atoms. *Phys. Rev. Lett.* **90**, 046808 (2003).
26. Repp, J., Meyer, G., Stojković, S., Gourdon, A. & Joachim, C. Molecules on insulating films: Scanning-tunneling microscopy imaging of individual molecular orbitals. *Phys. Rev. Lett.* **94**, 026803 (2005).
27. Nilius, N., Wallis, T., Persson, M. & Ho, W. Distance dependence of the interaction between single atoms: Gold dimers on NiAl(110). *Phys. Rev. Lett.* **90**, 196103 (2003).
28. Sonnleitner, T., Swart, I., Pavliček, N., Pöllmann, A. & Repp, J. Molecular symmetry governs surface diffusion. *Phys. Rev. Lett.* **107**, 186103 (2011).
29. Kawai, S. *et al.* Atom manipulation on an insulating surface at room temperature. *Nature Commun.* **5**, 4403 (2014).
30. Repp, J., Meyer, G., Paavilainen, S., Olsson, F. & Persson, M. Scanning tunneling spectroscopy of Cl vacancies in NaCl films: Strong electron-phonon coupling in double-barrier tunneling junctions. *Phys. Rev. Lett.* **95**, 225503 (2005).
31. Zielasek, V., Hildebrandt, T. & Henzler, M. Surface color centers on epitaxial NaCl films. *Phys. Rev. B* **62**, 2912–2919 (2000).
32. Simon, B. The bound state of weakly coupled Schrödinger operators in one and two dimensions. *Ann. Phys.* **97**, 279–288 (1976).
33. Gross, L., Mohn, F., Moll, N., Liljeroth, P. & Meyer, G. The chemical structure of a molecule resolved by atomic force microscopy. *Science* **325**, 1110–1114 (2009).
34. Mohn, F., Schuler, B., Gross, L. & Meyer, G. Different tips for high-resolution atomic force microscopy and scanning tunneling microscopy of single molecules. *Appl. Phys. Lett.* **102**, 073109 (2013).
35. The 2NN divacancy was less stable than the divacancies with larger separations.
36. Bennewitz, R. *et al.* Ultrathin films of NaCl on Cu(111): A LEED and dynamic force microscopy study. *Surf. Sci.* **438**, 289–296 (1999).
37. Repp, J., Meyer, G. & Rieder, K.-H. Snell’s law for surface electrons: Refraction of an electron gas imaged in real space. *Phys. Rev. Lett.* **92**, 036803 (2004).
38. Gross, L. *et al.* Investigating atomic contrast in atomic force microscopy and Kelvin probe force microscopy on ionic systems using functionalized tips. *Phys. Rev. B* **90**, 155455 (2014).
39. Kresse, G. & Joubert, D. From ultrasoft pseudopotentials to the projector augmented-wave method. *Phys. Rev. B* **59**, 1758–1775 (1999).
40. Blöchl, P. E. Projector augmented-wave method. *Phys. Rev. B* **50**, 17953–17979 (1994).
41. Kresse, G. & Furthmüller, J. Efficient iterative schemes for ab initio total-energy calculations using a plane-wave basis set. *Phys. Rev. B* **54**, 11169–11186 (1996).
42. Thonhauser, T. *et al.* Van der waals density functional: Self-consistent potential and the nature of the van der waals bond. *Phys. Rev. B* **76**, 125112 (2007).
43. Klimeš, J. c. v., Bowler, D. R. & Michaelides, A. Van der Waals density functionals applied to solids. *Phys. Rev. B* **83**, 195131 (2011).
44. See Supporting Information at <http://>.
45. Lyo, I.-W. & Avouris, P. Negative differential resistance on the atomic scale: Implications for atomic scale devices. *Science* **245**, 1369–1371 (1989).
46. At positive voltages, the NDC arises from the increase of the tunnel barrier for resonant tunneling through the VS with voltages greater than the VS²⁶; for negative voltages the NDC stems from a nonuniform tip density of states⁴⁵.

ACKNOWLEDGMENTS

We thank R. Allenspach for comments and acknowledge financial support from the ERC Advanced Grant CEMAS (agreement no. 291194) and the EU projects PAMS (610446) and QTea (317485). Allocation of computer resources through SNAC and CSC is gratefully acknowledged.

AUTHOR CONTRIBUTIONS

All authors contributed to the preparation of the paper. B.S., N.P., L.G, G.M. and J.R. conducted the experiments. M.P. and S.P. developed the coupling models and performed the DFT calculations.

ADDITIONAL INFORMATION

Correspondence and requests for materials should be addressed to B.S. (e-mail: bsc@zurich.ibm.com).

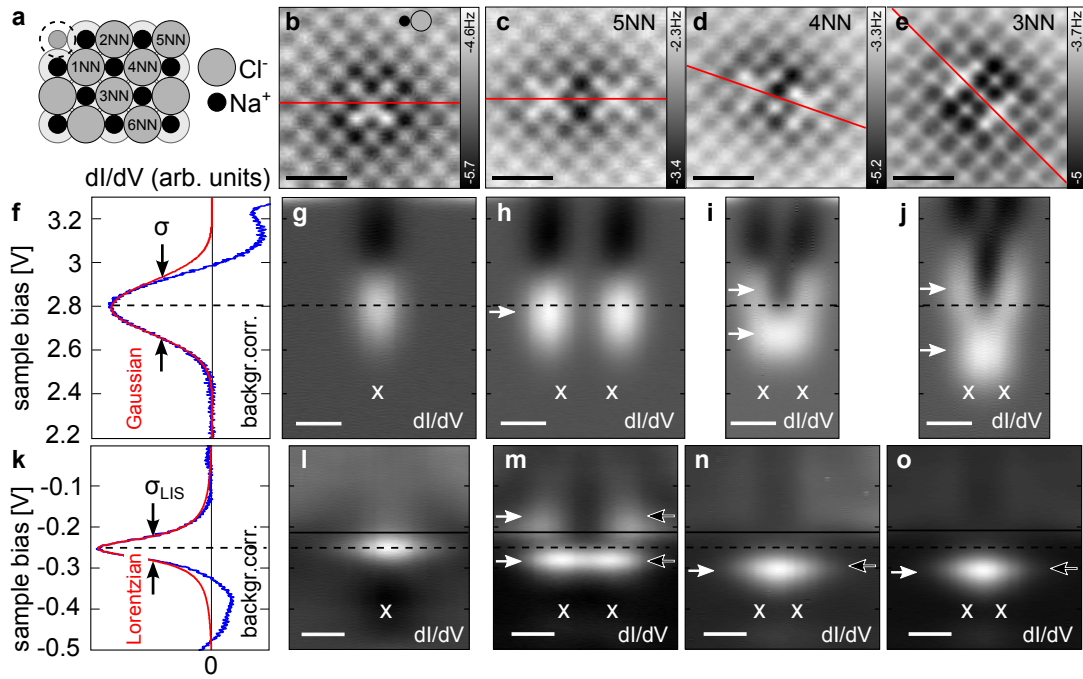


FIG. 1. **Vacancy states and localized interface-states of Cl divacancies.** **a** NaCl bilayer model with a Cl vacancy (dashed circle) and its nearest Cl neighbours indicated. **b-e** Constant-height CO tip AFM images of a single Cl vacancy (b) and divacancies in the 5NN (c), 4NN (d) and 3NN (e) configurations. **f** Background-subtracted dI/dV spectrum of the monovacancy state (VS) peak with a Gaussian fit in red. **g-j** $dI/dV(x, V)$ maps along the red lines in b-e (same V scale as in f). Peaks in dI/dV are displayed as bright, whereas the darkest areas mark regions of negative differential conductance (NDC)⁴⁶. The dashed line indicates the monovacancy VS peak position. **k** Background-subtracted dI/dV spectrum of the localized interface-state (LIS) of a monovacancy with a Lorentzian fit in red. **l-o** $dI/dV(x, V)$ maps along the red lines indicated in b-e, respectively (same V scale as in k). The dashed line indicates the monovacancy LIS peak position and the solid line the interface-state band onset. White crosses indicate the vacancy positions. White arrows mark the peak positions of the observed dI/dV resonances. Black arrows in m-o mark the peak positions of the calculated LDOS using the σ -wave multiple scattering model. All STS measurements were acquired with Cu tips. Scale bars: 10 Å.

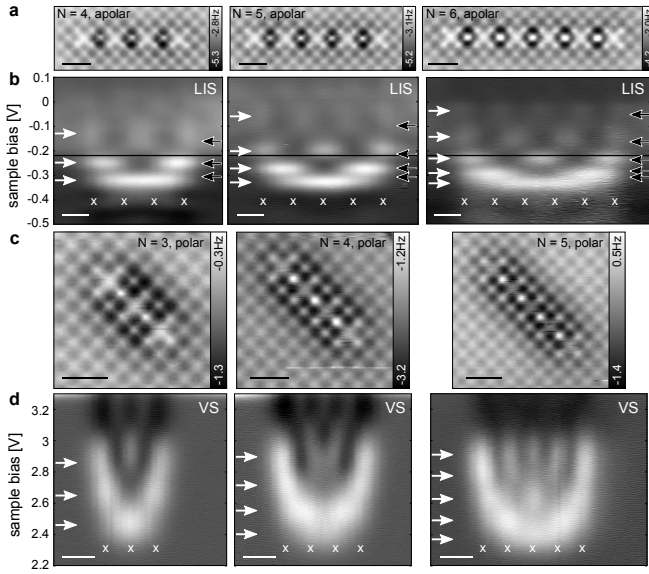


FIG. 2. **Vacancy states and localized interface-states of Cl vacancy chains.** **a** Constant-height CO tip AFM images of Cl vacancy chains with $N = 4, 5, 6$ vacancies in the 5NN configuration (apolar direction). **b** Corresponding $dI/dV(x, V)$ maps of the LISs along the chains. The continuous line indicates the interface-state band onset. White arrows mark the peak positions of the observed dI/dV resonances, and black arrows mark the peak positions of the calculated LDOS. **c** Constant-height CO tip AFM images of Cl vacancy chains with $N = 3, 4, 5$ vacancies in the 3NN configuration (polar direction). **d** Corresponding $dI/dV(x, V)$ maps of the VSs along the chains. White crosses mark the positions of the vacancies and the white arrows dI/dV peaks. Scale bars: 10 \AA .

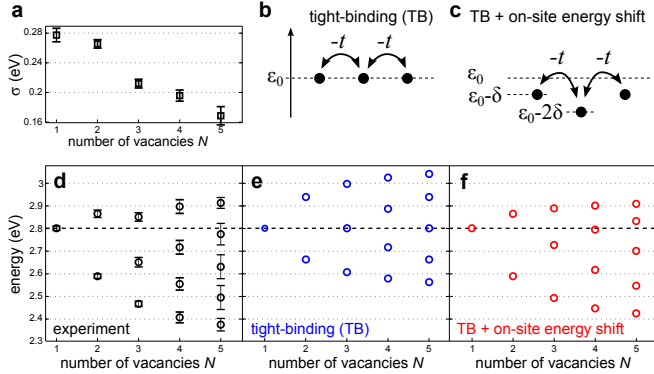


FIG. 3. **Tight-binding models.** **a** Experimental VS broadening σ as a function of the 3NN chain length. **b** Tight-binding (TB) model for a $N = 3$ chain. **c** TB model including the electrostatic on-site energy shift between nearest neighbours. **d** Experimental VS energies as a function of the 3NN chain length. **e** TB model energies obtained by fitting the on-site energy $\epsilon_0 = 2.8 \text{ eV}$ and hopping term $t = 0.14 \text{ eV}$ to the experimental mono- and divacancy VS energies shown in d. **f** TB model accounting for a shift of the on-site energy ($\delta = 0.07 \text{ eV}$) due to the electrostatic interaction between nearest neighbours.

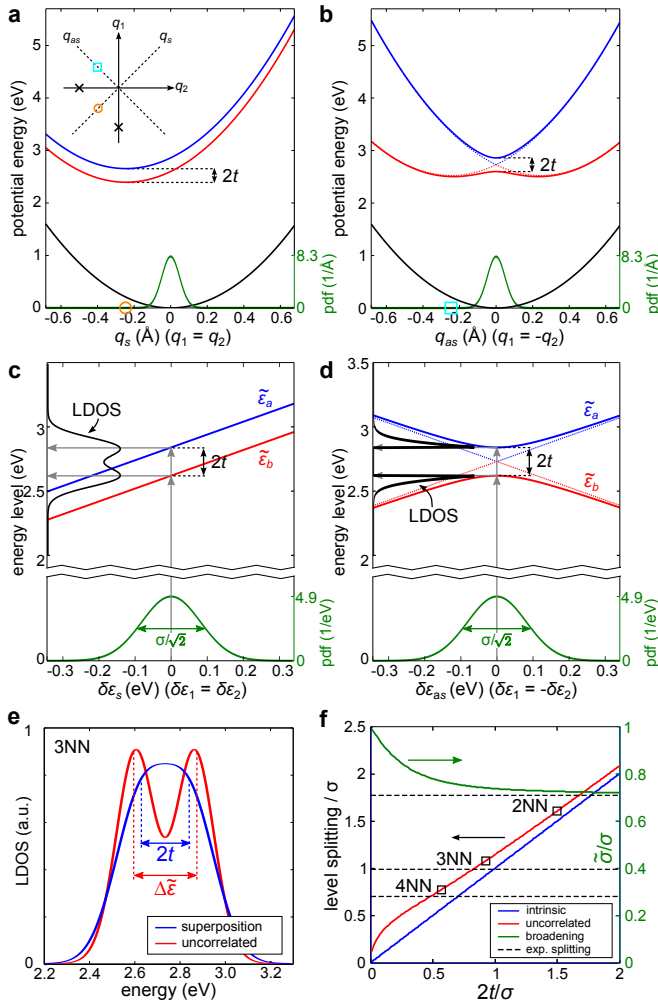


FIG. 4. Lineshapes of vacancy states of a Cl divacancy. **a,b** Calculated adiabatic potential energy surfaces (PESs) of the electronic ground-state (black) and the electronically excited and singly occupied divacancy states (red and blue) as a function of symmetric q_s (**a**) and antisymmetric q_{as} (**b**) phonon displacements. The vibrational ground-state probability distribution functions (pdf) of q_s (**a**) and q_{as} (**b**) are indicated by the green curves. Here, $2t$ is the intrinsic electronic level splitting. The inset in (**a**) shows q_s and q_{as} in terms of the displacements q_1 and q_2 of the two Einstein modes each associated with a vacancy. The black crosses mark equilibrium displacements of vacancy 1 and 2 when the divacancy is occupied by a single electron. **c,d** Energy-level diagram for the divacancy states as a function of symmetric $\delta\varepsilon_s$ (**c**) and antisymmetric $\delta\varepsilon_{as}$ fluctuations (**d**) of the monovacancy energies induced by the phonon motion. The vertical gray arrows indicate the electron-attachment process and the black curves the resulting LDOS. **e** Calculated LDOS of the 3NN divacancy for uncorrelated vacancy energy fluctuations (red) compared to a superposition of two Gaussians separated by $2t$ and each with a broadening σ (blue). $\Delta\tilde{\varepsilon}$ denotes the level splitting for uncorrelated vacancy energy fluctuations. **f** Scaled level splitting $\Delta\tilde{\varepsilon}/\sigma$ as obtained from a Gaussian fit to the calculated lineshapes of the divacancy states for uncorrelated vacancy energy fluctuations (red) compared to the intrinsic splitting (blue) as a function of the scaled intrinsic level splitting $2t/\sigma$. The calculated and observed scaled splittings for different divacancy configurations are indicated by black squares and dashed horizontal lines, respectively. The green curve shows the apparent level broadening $\tilde{\sigma}$ for uncorrelated vacancy energy fluctuations.